Published in final edited form as:
Opt Lett. 2019 March 01; 44(5): 1186–1189. doi:10.1364/OL.44.001186.

Local wavefront mapping in tissue using computational adaptive optics OCT

Fredrick A. South[1,2], **Yuan-Zhi Liu**[1], **Pin-Chieh Huang**[1,3], **Tabea Kohlfarber**[1,4], **Stephen A. Boppart**[1,2,3,5,*]

[1]Beckman Institute for Advanced Science and Technology, University of Illinois at Urbana-Champaign, Urbana, Illinois 61801, USA

[2]Department of Electrical and Computer Engineering, University of Illinois at Urbana-Champaign, Urbana, Illinois 61801, USA

[3]Department of Bioengineering, University of Illinois at Urbana-Champaign, Urbana, Illinois 61801, USA

[4]Institute of Biomedical Optics, Universität zu Lübeck, Peter-Monnik-Weg 4, 23562 Lübeck, Germany

[5]Carle Illinois College of Medicine, University of Illinois at Urbana-Champaign, Urbana, Illinois 61801, USA

Abstract

The identification and correction of wavefront aberrations is often necessary to achieve high-resolution optical images of biological tissues, as imperfections in the optical system and the tissue itself distort the imaging beam. Measuring the localized wavefront aberration provides information on where the beam is distorted and how severely. We have recently developed a method to estimate the single-pass wavefront aberrations from complex optical coherence tomography (OCT) data. Using this method, localized wavefront measurement and correction using computational OCT was performed in *ex vivo* tissues. The computationally measured wavefront varied throughout the imaged OCT volumes and, therefore, a local wavefront correction outperformed a global wavefront correction. The local wavefront measurement was also used to generate tissue aberration maps. Such aberration maps could potentially be used as a new form of tissue contrast.

In high-resolution imaging applications, the imaging beam is often distorted due to imperfect optics or refractive index variations in the imaged sample. Knowledge of the local wavefront variation in the imaged sample is useful for a variety of purposes. The most obvious application is localized aberration correction to improve image quality. Beyond direct image improvement, a map of the local wavefront variation can be used to estimate the size of the isoplanatic patch for different tissue types, determining the maximum area over which a single aberration correction can be applied [1]. This information is useful for speeding up both hardware and computational aberration correction, as fewer total corrections need to be measured and applied. A local wavefront map could also be used to

---

[*] Corresponding author: boppart@illinois.edu.

determine the spatially varying aberrations of an optical imaging system design. Such information could be used to assess the performance of an optical system to determine if image quality is sufficient within the imaging region.

Adaptive optics for wavefront measurement and correction is traditionally performed using hardware components, such as a wavefront sensor and deformable mirror, or deformable mirror alone [2,3]. However, aberrations can also be corrected by digitally modifying the phase of coherent backscattered light [4]. Using the complex-valued data acquired by optical coherence tomography (OCT), computational adaptive optics (CAO) has been used to correct aberrations for imaging a variety of biological tissues, including *in vivo* photoreceptors in the human eye [5,6]. As with traditional adaptive optics, CAO only corrects the wavefront over an isoplanatic volume where the wavefront error is relatively constant. The use of CAO to correct isoplanatic regions of interest within a single dataset was first published in Ref. [7], and subsequently demonstrated in the human eye [8]. We have recently developed a CAO method for estimating the single-pass wavefront aberration directly from the complex OCT data [9]. Here we present the use of this method for localized measurements, correction, and mapping of wavefront variations in biological tissue.

The CAO wavefront measurement method is briefly outlined here, and further details can be found in Ref. [9]. The complex-valued OCT signal at each transverse location $(x, y) = \mathbf{r}_{\parallel}$ and depth location z is defined as $S(\mathbf{r}_{\parallel}, z)$. Using the two-dimensional Fourier transform, the signal can be represented in the transverse spatial frequency domain as $\widetilde{S}(\mathbf{q}_{\parallel}, z)$, where $(\tilde{\ })$ denotes the two-dimensional Fourier transform in the lateral dimension, and $\mathbf{q}_{\parallel}$ represents transverse spatial frequency. The aberrated OCT signal at a particular depth z_i can be approximated as

$$\widetilde{S}_{\mathrm{A}}(\mathbf{q}_{\parallel}, z_i) = H_{\mathrm{A}}(\mathbf{q}_{\parallel}, z_i)\widetilde{S}(\mathbf{q}_{\parallel}, z_i), \tag{1}$$

where H_A is the aberrated transfer function of the imaging system at a particular depth within the sample.

The aberrated transfer function is proportional to the auto-convolution of the aberrated pupil:

$$H_{\mathrm{A}}(\mathbf{q}_{\parallel}, z_i) \propto G(\mathbf{q}_{\parallel}, z_i) * G(\mathbf{q}_{\parallel}, z_i), \tag{2}$$

where

$$G(\mathbf{q}_{\parallel}, z_i) = \mid G(\mathbf{q}_{\parallel}, z_i) \mid \exp[\phi_g(\mathbf{q}_{\parallel}, z_i)]. \tag{3}$$

The aberration correction filter is given by

$$H_{\mathrm{AC}}(\mathbf{q}_{\parallel}, z_i) = \exp(-i \arg[G(\mathbf{q}_{\parallel}, z_i) * G(\mathbf{q}_{\parallel}, z_i)]), \tag{4}$$

and applied to the aberrated OCT signal to retrieve the aberration corrected OCT signal

$$\tilde{S}_{\mathrm{AC}}(\mathbf{q}_{\parallel}, z_i) = H_{\mathrm{AC}}(\mathbf{q}_{\parallel}, z_i)\tilde{S}_{\mathrm{A}}(\mathbf{q}_{\parallel}, z_i)\,. \tag{5}$$

This can then be Fourier transformed back to the spatial domain to give the aberration corrected OCT depth image $S_{\mathrm{AC}}\,(\mathbf{r}_{\parallel}, z_i)$.

The desired information in this application is the wavefront of the single-pass transfer function, ϕ_g. This can be estimated by finding the wavefront that maximizes the image quality of the corrected image according to

$$\widehat{\Phi}_g(\mathbf{q}_{\parallel}, z_i) = \underset{\phi_g}{\mathrm{argmax}}\,\mathscr{I}(S_{\mathrm{AC}}(\mathbf{r}_{\parallel}, z_i)), \tag{6}$$

where $S_{\mathrm{AC}}(\mathbf{r}_{\parallel}, z_i)$ is calculated according to Eqs. (4) and (5), and $\mathscr{I}()$ indicates one of a variety of image sharpness metrics [10]. This wavefront measurement can be made globally over the entire image plane, or locally over an isoplanatic patch where the wavefront aberrations are anticipated to be approximately the same.

To demonstrate wavefront measurements in biological tissue, *ex vivo* samples were imaged using a spectral domain OCT system described previously, modified to use a superluminescent diode with a wavelength range of 1325 ± 50 nm [11]. The global wavefront estimate was calculated over the 2 × 2 mm transverse field-of-view (FOV). The local wavefront was estimated within a 200 × 200 μm sliding window. The choice of window size was determined by two factors. First, the window size must be large enough to include the entire aberrated point-spread function. Secondly, it must be large enough for the window to include sufficient structural information such that the sharpness metric is not dominated by speckle noise [12]. A window of 200 × 200 μm was experimentally determined to be appropriate for this imaging system across multiple samples of interest.

The wavefront estimate summarized in Eq. (6) was calculated using the MATLAB parallel computing and optimization toolboxes running on an Intel Core i7-5960. The computation time was 88.5 ms for a subregion and 10.08 s for the full FOV. The sliding window step size was 33.6 μm, totaling 55 × 55 windows over the full FOV. When compiling the locally corrected subregions into a composite image, the central pixels of each subregion were used so that edge effects were not present in the composite image.

Figure 1 shows global and local aberration correction in an *ex vivo* mouse brain slice of the cortex. Because the aberrations vary across the FOV, a global CAO correction may improve one region while degrading another. The globally corrected image and corresponding wavefront are shown in Fig. 1(a). The edge of the hippocampus is aberrated and out of focus prior to wavefront correction [Fig. 1(b)]. The global correction improves the peak signal and point-spread function of this subregion [Fig. 1(c)]. However, the myelinated nerve bundles [Fig. 1(f)] are near focus and relatively unaberrated to begin with. As a result, the global correction degrades the image quality for this subregion [Fig. 1(g)].

A local measurement takes the spatial variation of the wavefront into account and improves each region independently. The locally corrected images in Figs. 1(d) and 1(h) show an improved peak signal and point-spread function relative to their globally corrected counterparts. The locally measured wavefronts in Figs. 1(e) and 1(i) demonstrate the significant difference in the correction between the two locations. The comparison between global and local correction is further quantified in Table 1, where the improvement in the intensity squared sharpness metric is given for the entire FOV and the two subregions indicated by the green and red squares in Fig. 1(a). The region-specific aberration measurements and correction lead to better performance in each of the three cases.

This local measurement can be performed across the entire imaging region to generate an aberration map. Assuming negligible anisoplanacity of the optical system, this provides insight into how much the tissue itself impacts the optical wavefront and image quality. Figure 2 shows OCT imaging and local wavefront measurements in *ex vivo* chicken breast tissue. Cross-sectional and *en face* images are shown in Figs. 2(a) and 2(b), respectively. The dashed yellow line indicates the depth from which the *en face* image is taken, and the arrowhead is included to indicate the relative orientation of the cross-sectional and *en face* images. Figure 2(c) maps the spatial variation of the local wavefront RMS over the *en face* plane. The surface of the muscle tissue was uneven. As a result, the imaging beam at a given depth plane traveled through varying amounts of tissue across the FOV. As the beam propagates through the tissue, refractive index variations distort the optical wavefront such that the wavefront RMS is much greater where the beam has traveled through more tissue. This can be seen in the gradient of the wavefront RMS in Fig. 2(c). This demonstrates that different paths through the same tissue type can lead to local variation in the optical wavefront.

Wavefront variation can also be caused by differences in tissue type. For example, dense tissues may aberrate the imaging beam more severely than tissues that are more optically transparent. This is demonstrated in Fig. 3, where adipose and muscle tissues are adjacent within the same imaging volume. Figures 3(a) and 3(b) show cross-sectional and *en face* OCT images. The spatial variation of the local wavefront is mapped in Fig. 3(c). Here the wavefront RMS is shown without defocus to highlight the wavefront variation, as defocus was similar across the FOV due to the relatively flat tissue surface. Despite the flat tissue surface, the wavefront RMS varies significantly across the FOV, because the muscle tissue distorts the imaging beam more severely than the adipose tissue.

The difference in wavefront RMS for the two tissue types may be interpreted as a result of refractive index variation within the interrogation volume [13]. The interrogation area is the transverse area over which the imaging beam must scan to measure the spatial frequency data of a given point in the imaging volume. For a point-scanning beam, the interrogation area is simply the size of the point-spread function at that depth. The measured wavefront is impacted by the refractive index variation of the tissue at and above the given depth plane. The concatenation of the interrogation area at the relevant depths gives a three-dimensional interrogation volume. Refractive index variations within this volume lead to wavefront errors. Compared to the densely packed muscle fibers, the refractive index of the adipocytes has less variation throughout the interrogation volume, resulting in reduced wavefront RMS.

The choice of image sharpness metric in Eq. (6) is important when considering the optimization of various image types [10]. A family of image sharpness metrics has been proposed where the signal intensity is raised to the power γ:

$$\sum_{x, y} I^{\gamma}(x, y)\,. \tag{7}$$

While this metric is maximized in the absence of aberrations, the optimization performance of the metric can vary quite dramatically, depending on the characteristics of the image and choice of γ. Images that are expected to have bright point-like features are more easily optimized by image sharpness metrics with large powers, such as $\gamma \geq 2$. This emphasizes the improvement in contrast at high intensities and can perform well for point-like objects, such as photoreceptors in the retina [14]. However, images with dark features within a scattering background are better optimized by sharpness metrics with small powers, such as $\gamma < 1$. The negative entropy metric,

$$\sum_{x, y} I(x, y)\ln[I(x, y)], \tag{8}$$

is also widely used and behaves similarly to the Eq. (7) power metric with $\gamma = 1.1$.

Several options for the optimization metric in Eq. (6) were tested using the dataset presented in Fig. 2. Each 200 × 200 μm subregion was independently optimized. The improvement in the $\gamma = 2$ intensity squared metric of the composite corrected image was used as a common standard to measure the sharpness improvement. The optimization procedure was allowed 10 * N function evaluations at each subregion, where N was the number of Zernike weights being optimized (N = 12, including 2nd,- 3rd-, and 4th-order aberrations) [15]. Table 2 shows the improvement in sharpness and the percent of subregions which converged in the allotted number of function evaluations. Of the tested metrics, the negative entropy metric of Eq. (8) showed the best performance and was determined to be the most appropriate for the scattering biological tissues in this Letter.

As mentioned previously, the window size used for wavefront measurements must contain a sufficient image structure to perform a successful image sharpness optimization. Even with a 200 × 200 μm window size, there may be some subregions in which there is a negligible signal or where the sample structure is homogeneous relative to the resolution of the imaging system. Without a significant sample structure, the optimization is performed on a subregion with intensity variations dominated by noise. In the case of a homogeneously scattering subregion, this can lead to artificially inflated RMS wavefront values.

To determine a level of trust for a local wavefront measurement, the intrinsic sharpness of that region can be estimated from the aberrated image. Because the autocorrelation is not impacted by the wavefront error, it can be used to estimate the aberration-free image sharpness [10]. For this Letter, the variance of the autocorrelation was used, excluding the DC term, and normalized by the total subregion intensity. The sharpness estimate can be used to mask out areas of the wavefront map that do not have a significant underlying image structure. This was not necessary for the chicken breast data, which had a sufficient image structure throughout the dataset due to the striations of the muscle fibers. However, the brain slice images contained large areas with low intrinsic sharpness. Such areas can be masked, as shown in Fig. 4(b), where the estimated image sharpness is mapped to the brightness, and the wavefront RMS is mapped to color. Here the brightness indicates a level of trust in the wavefront estimate. The estimated sharpness and corresponding RMS value for each subregion are shown in Fig. 4(c), highlighting the fact that runaway RMS values can occur in areas of low intrinsic sharpness. Therefore, wavefront measurements of these regions should be treated with a healthy skepticism.

Local wavefront measurement and correction using CAO OCT provides improved image correction when compared to a global CAO correction. When the image size is significantly greater than the isoplanatic patch, the global correction will be suboptimal and may even degrade the image quality in certain places. Locally applied CAO optimizes the image quality throughout the FOV, which can sometimes mean leaving well-focused image regions relatively untouched.

Additionally, CAO can be used to generate an aberration map to illustrate where the tissue distorts the optical wavefront. Differences in wavefront RMS can arise from different paths through the same tissue type. More interestingly, different tissue types impact the wavefront in unique ways. With further research, it may be possible to use this aberration contrast to distinguish tissue types in certain biomedical applications. In general, computational wavefront measurements can be explored for any application where hardware-based wavefront measurements have been found to be useful.

Acknowledgment.

The authors thank Darold Spillman for technical support. F. South was supported in part by an ECE Yang fellowship. Additional information can be found at http://biophotonics.illinois.edu.

Funding. National Institutes of Health (NIH) (R01 CA213149, R01 EB013723, R01 EB023232); Air Force Office of Scientific Research (AFOSR) (FA9550-17-1-0387).

REFERENCES

1. Zeng J, Mahou P, Schanne-Klein M-C, Beaurepaire E, and Débarre D, Biomed. Opt. Express 3, 1898 (2012). [PubMed: 22876353]
2. Booth MJ, Light Sci. Appl 3, e165 (2014).
3. Jonnal RS, Kocaoglu OP, Zawadzki RJ, Liu Z, Miller DT, and Werner JS, Invest. Ophthalmol. Vis. Sci 57, OCT51 (2016). [PubMed: 27409507]
4. Adie SG, Graf BW, Ahmad A, Carney PS, and Boppart SA, Proc. Natl. Acad. Sci 109, 7175 (2012). [PubMed: 22538815]
5. Shemonski ND, South FA, Liu Y-Z, Adie SG, Scott Carney P, and Boppart SA, Nat. Photonics 9, 440 (2015). [PubMed: 26877761]
6. Liu Y-Z, South FA, Xu Y, Carney PS, and Boppart SA, Biomed. Opt. Express 8, 1549 (2017). [PubMed: 28663849]
7. Kumar A, Kamali T, Platzer R, Unterhuber A, Drexler W, and Leitgeb RA, Biomed. Opt. Express 6, 1124 (2015). [PubMed: 25908999]
8. Hillmann D, Spahr H, Hain C, Sudkamp H, Franke G, Pfäffle C, Winter C, and Hüttmann G, Sci. Rep 6, 35209 (2016). [PubMed: 27762314]

9. South FA, Liu Y-Z, Bower AJ, Xu Y, Carney PS, and Boppart SA, J. Opt. Soc. Am. A 35, 466 (2018).
10. Fienup JR and Miller JJ, J. Opt. Soc. Am. A 20, 609 (2003).
11. Shemonski ND, Ahn SS, Liu Y-Z, South FA, Carney PS, and Boppart SA, Biomed. Opt. Express 5, 4131 (2014). [PubMed: 25574426]
12. Paxman RG and Marron JC, Proc. SPIE 0976, 37 (1988).
13. Shemonski ND, Adie SG, Liu Y-Z, South FA, Carney PS, and Boppart SA, Opt. Express 22, 19183 (2014). [PubMed: 25321004]
14. Pande P, Liu Y-Z, South FA, and Boppart SA, Opt. Lett 41,3324 (2016). [PubMed: 27420526]
15. Lakshminarayanan V and Fleck A, J. Mod. Opt 58, 1678 (2011).

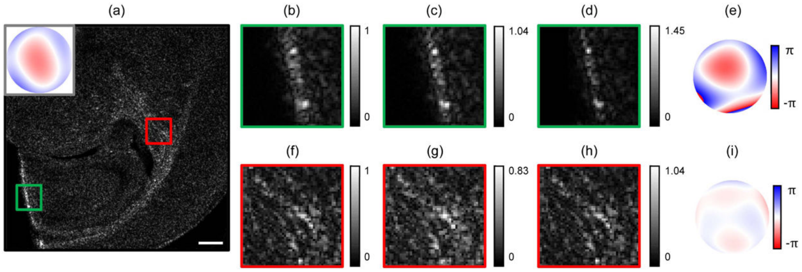

Fig. 1.

Measurement and correction of aberrations in an *ex vivo* mouse brain slice. (a) Corrected depth image when CAO is applied to the entire FOV. The inset shows the global wavefront. (b)–(d) OCT images from Subregion 1 corresponding to the green square in (a). (f)–(h) OCT images from Subregion 2 corresponding to the red square in (a). (b), (f) Uncorrected OCT images. (c), (g) Globally corrected images using the wavefront from (a). (d), (h) Locally corrected images. (e), (i) Local wavefront measurements used to obtain the images in (d) and (h), respectively. The image intensities are normalized to the peak amplitude of the uncorrected OCT subregions. The scale bar and subregion widths are 200 μm.

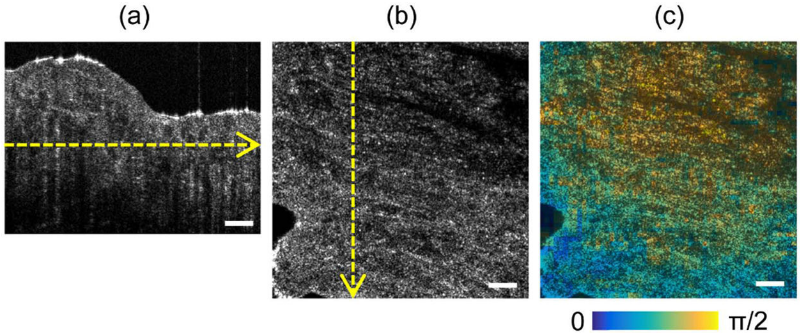

Fig. 2.

Wavefront measurement and correction in *ex vivo* chicken breast tissue. (a) OCT cross section showing an uneven tissue surface. (b) Composite *en face* image of locally corrected subregions, taken at the depth plane indicated by the yellow line in (a). (c) Map of the local wavefront RMS across the *en face* image (b). The scale bar is 200 µm.

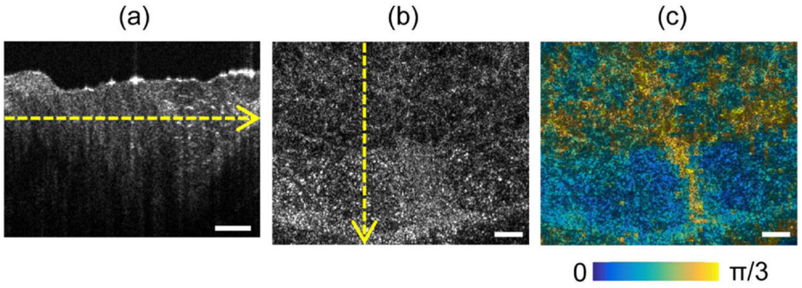

Fig. 3.

Wavefront measurement and correction in *ex vivo* chicken breast tissue. (a) OCT cross section showing the muscle (left) and adipose (right) tissue types. (b) Composite *en face* image of locally corrected subregions, taken at the depth plane indicated by the yellow line in (a). (c) Map of the local wavefront RMS across the *en face* image (b), excluding defocus. The scale bar is 200 µm.

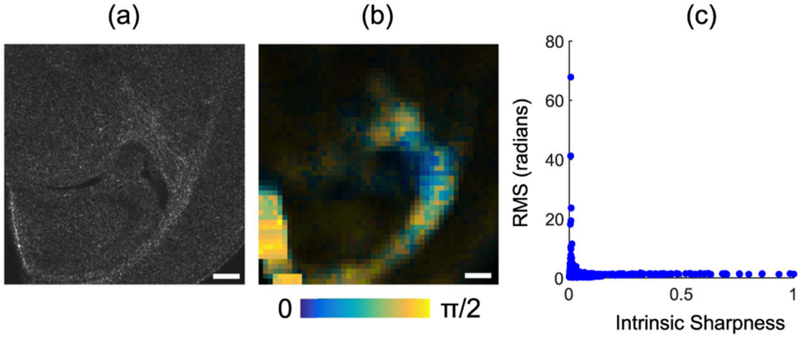

Fig. 4.

Wavefront map for an *ex vivo* mouse brain slice. (a) Composite depth image of locally corrected subregions. (b) Local wavefront RMS, with the brightness mapped to estimated image sharpness. (c) Estimated image sharpness versus computational wavefront RMS. Each data point represents the estimated sharpness and RMS of one subregion. The scale bar is 200 μm.

Table 1.

Image Sharpness Change for Global and Local Wavefront Correction in Fig. 1

Correction	Full FOV	Subregion 1 (Green Square)	Subregion 2 (Red Square)
Global	+ 10.5%	+30.0%	−14.8%
Local	+34.5%	+83.0%	+1.3%

Table 2.

Image Sharpness Improvement and Wavefront Measurement Convergence Rates on Fig. 2 for Select Metrics

	$\gamma = 4$	$\gamma = 2$	$\gamma = 0.5$	$I \ln(I)$
Sharpness Improvement	40%	40%	41%	44%
Convergence	75%	78%	71%	90%